Elucidating the Role of Support Oxygen in the Water–Gas Shift Reaction Over Ceria-Supported Gold Catalysts Using *Operando* Spectroscopy

Christian Schilling, Christian Hess*

Eduard-Zintl-Institut für Anorganische und Physikalische Chemie, Technische Universität Darmstadt, Alarich-Weiss-Str. 8, 64287 Darmstadt, Germany

*hess@pc.chemie.tu-darmstadt.de

Graphical Abstract

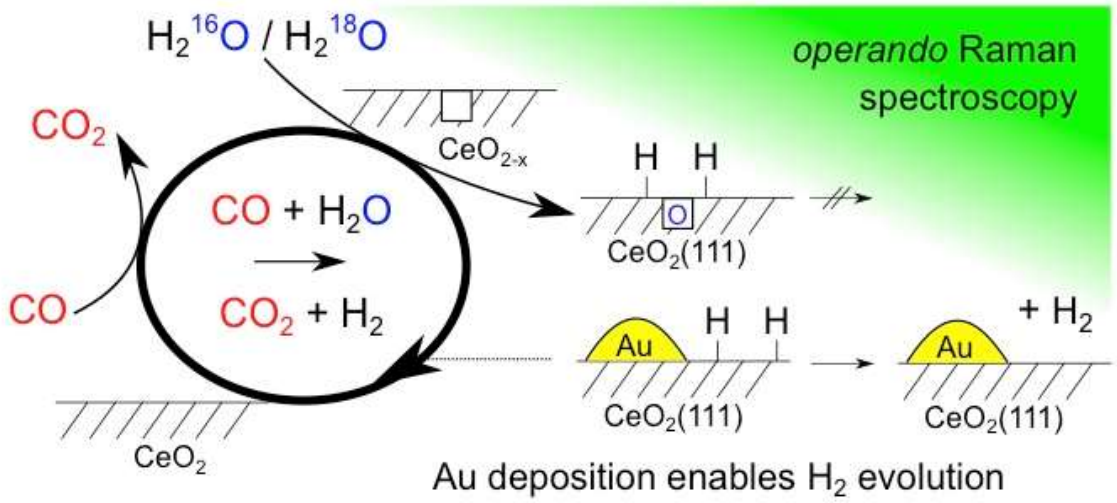

Abstract

Supported-metal (Au, Pt) ceria-based catalysts are considered as promising candidates for the water–gas shift (WGS) reaction at low temperatures. Two main mechanisms have been proposed in the literature, the redox and associative mechanisms. A key step in both mechanisms has been considered to be the cleavage of O–H bonds. In this mechanistic study the role of surface and bulk oxygen species involved in the WGS reaction over ceria supported gold catalysts (Au/CeO_2) was elucidated directly using *operando* Raman spectroscopy combined with isotope labelling and supported by DFT+U calculations. Exposure of Au/CeO_2 to pure $H_2{}^{18}O$ results in a complete replacement of surface ^{16}O ions by ^{18}O ions as rationalized by dissociative adsorption of $H_2{}^{18}O$ in the presence of a surface oxygen vacancy and a subsequent backward reaction restoring lattice oxygen as ^{18}O and releasing $H_2{}^{16}O$. This reaction pathway is accessible even in the absence of CO. Exposure to reaction conditions leads to (i) a complete disappearance of the Ce–O surface modes due to hydroxyl formation (ii) a Raman F_{2g} redshift due to reduction of the ceria subsurface, leading to a change in stoichiometry from $CeO_{1.947-x}$ (in argon) to $CeO_{1.873-x}$ (in $CO/H_2{}^{16}O$), (iii) large amounts of ^{18}O in the subsurface of the ceria support due to oxygen transfer from the surface to the ceria subsurface, highlighting the oxygen dynamics of the ceria support. While the results of this study are fully consistent with a redox mechanism involving a reaction pathway for replenishment of surface oxygen ions O^{2-} from terminal hydroxyl groups (O–H) accessible also in the absence of CO in the gas phase, other reaction mechanisms cannot be ruled out.

Keywords: ceria, gold, water-gas shift, *operando* Raman spectroscopy, isotope exchange, reaction mechanism

1. Introduction

There has recently been increased interest in the low temperature water-gas shift reaction (LT-WGS) to reduce the amount of CO and increase the amount of hydrogen after steam reforming for hydrogen production, e.g., for fuel cells. [1] The WGS reaction ($CO + H_2O \rightarrow CO_2 + H_2$) is equilibrium limited and exothermic ($\Delta H° = -41.1$ kJ/mol) requiring catalysts active at low temperatures to achieve low CO concentrations (<0.5 %). [1] The industrial LT WGS reaction catalyst $Cu/ZnO/Al_2O_3$ is pyrophoric and shows a low thermal stability. [1] As an alternative, low loaded noble metal–based catalysts have been suggested and recent studies on the WGS reaction over supported noble metals (Pt, Au) have shown that reducible oxides such as ceria can greatly improve the catalytic activity at low temperatures. [2] [3]

While there is consensus about the bifunctionality of metal oxide–supported noble metal catalysts in the WGS reaction, i.e., the participation of both the metal particles and the oxidic support material, the detailed reaction mechanism is a matter of debate. Two types of mechanisms have been proposed in the literature for this reaction, a redox mechanism [2] and associative mechanisms. [4] [5] According to the redox mechanism, CO adsorbed on the metal phase is oxidized to CO_2 by lattice oxygen from the support, resulting in the formation of an oxygen vacancy, which is replenished by water, giving hydrogen after O–H bond cleavage. The associative mechanism is initiated by the interaction of adsorbed CO with terminal hydroxyl groups on the oxide support, leading to different intermediate species, and is completed by their decomposition to CO_2 and hydrogen. Proposed intermediates include formate [6-8], carbonate [9] [10] and carboxyl / carboxylate [11-14] species.

The redox mechanism was originally proposed for ceria supported noble metals (Pt, Pd, Rh) by Gorte and coworkers, [15] and later also for Au/ceria catalysts by Flytzani-Stephanopoulos and coworkers. [2] Using infrared spectroscopy to study Rh/CeO_2 catalysts, Shido and Iwasawa suggested an associative formate-based mechanism. [16] The experimental evidence for and

against such a formate mechanism was discussed in detail by Burch et al., who considered the experimental data available for the WGS reaction over a variety of metal oxide–supported noble metal catalysts (Rh/CeO_2, Pt/CeO_2, Au/CeO_2, $Au/Ce(La)O_2$, $Au/CeZrO_4$). [17] The authors concluded that formates were potentially the main intermediates only in the case of very low activity catalysts, whereas a major contribution of the formate mechanism remains to be proved for high activity catalysts. Similarly, based on their steady state isotopic transient kinetic analysis on Pt/CeO_2 and $Pt/Ce_xZr_{1-x}O_2$ catalysts, Kalamaras et al. concluded that formate should not be considered an important intermediate. [8] Common to both the redox and formate mechanisms is a water dissociation step. While previously water dissociation was reported to be energetically important in the WGS reaction, [5] [8] [12] [18] [19] according to work of Vecchietti et al. on Pt/CeO_2 the activation of water molecules was excluded as the rate-limiting step. [13] (Density functional theory) DFT calculations on $Au/CeO_2(111)$ suggest water dissociation to take place at the interface between Au and ceria with an oxygen vacancy nearby. [12] DFT studies on WGS reactions were briefly reviewed by Sauer and coworkers. [20] Based on DFT+U calculations on $Au/CeO_2(111)$, the O–H-bond cleavage in O-H groups, which is crucial in both the redox and formate mechanisms, was suggested to be energetically unfavorable with barriers >1eV. [5] Following a similar theoretical approach, King and coworkers had earlier proposed an associative carboxyl-based mechanism, [14] for which the rate-determining step was associated with the decomposition of COOH (1.08 eV). In direct relation to this study, Chen et al. calculated a reduced barrier to CO_2 formation by reaction of COOH with OH. [12]

Based on this brief account of previous results on the WGS reaction over metal oxide–supported noble metal catalysts it is apparent that, despite the progress in the field, a detailed understanding of the mode of operation of these catalysts is still lacking. In particular, there have been no studies directly addressing the surface oxygen dynamics of the support, despite its crucial role for all proposed mechanisms. Furthermore, while previous studies strongly

focused on surface-related processes, our recent findings for Au/CeO_2 catalysts have highlighted the importance of the subsurface dynamics for a detailed understanding of the catalytic behavior. [21]

In this work, we report on the role of the different surface and bulk oxygen species involved in the WGS reaction over ceria–supported gold catalysts. Detailed analysis of the oxygen and defect dynamics of the ceria support allows us to gain insight into the WGS reaction mechanism from a new perspective. For that purpose, we employed *operando* Raman spectroscopy, which had not been applied to WGS reaction conditions previously. The potential of *in situ* and *operando* Raman spectroscopy for mechanistic studies was demonstrated by performing isotope labeling experiments. To support our assignments and to gain additional mechanistic insight DFT+U calculations were used. [22]

2. Experimental Section

2.1. Catalyst Synthesis. The ceria support exposing the $CeO_2(111)$ surface termination (see TEM image in Figure S1 of the Supporting Information and discussion of the *operando* Raman spectra) was prepared as described previously.[23] [24] Briefly, $Ce(NO_3)_3$ (Alfa Aesar, 99.5%) was heated at a rate of 6°C/min, decomposed at 600°C for 12 h and subsequently allowed to cool to room temperature. The resulting powder was calcined again applying the same protocol. The specific surface area was determined to be 61 m^2/g by N_2 adsorption and use of the BET (Brunauer-Emmett-Teller) model. Gold was deposited onto the ceria support via deposition precipitation [25] [26] by first suspending 2 g CeO_2 in 300 mL deionized water and adjusting the pH value to 9 by a 0.1 M NaOH solution. Then an appropriate amount of a 10^{-3} M solution of $HAuCl_4 \cdot 3H_2O$ (Sigma Aldrich, 99.999%), adjusted to pH 9, was added to the ceria suspension to yield a nominal fraction of 0.5 wt% gold on ceria. After being kept at 65°C for 2 h, the suspension was allowed to cool down to room temperature, and treated for 30 min in a sonicator. The product was first centrifuged, then washed with 0.25% ammonia solution and water three times, and finally dried at 85°C for at least 48 h.

2.2. Transmission Electron Microscopy. For transmission electron microscopy (TEM) characterization of the CeO_2 support (see Figure S1) and Au/CeO_2 catalyst (see Figure S2), a JEOL JEM-2100F (Tokyo, Japan) microscope was employed, that was equipped with a Schottky field emitter operating at a nominal acceleration voltage of 200 kV. Energy dispersive X-ray (EDX) spectra were recorded on an Oxford X-MAX 80 silicon drift detector (Oxford Instruments NanoAnalysis, High Wycombe, UK) attached to the JEM-2100F. For sample preparation a small amount of powder was dispersed in ethanol using an ultrasound bath (Bandelin) for approximately 30 s. After the dispersion had settled for a short time, a droplet of the dispersion was applied to a holey carbon grid (Plano); the grid was coated with carbon (Bal-Tec MED010) to avoid charging under the incident electron beam.

2.3. X-ray Photoelectron Spectroscopy. For X-ray photoelectron spectroscopy (XPS) a modified Leybold-Heraeus LHS/SPECS EA200 system was employed. XP spectra were recorded with a Mg Kα source (1253.6 eV, 168 W) under UHV conditions (see Figure S3). Calibration was done based on the Au 4f signal of a gold foil at 84.0 eV and the Cu 2p signal of a copper plate at 932.7 eV. [27] To account for sample charging the Ce3d u‴ signal was set to 916.7 eV, [28] corresponding to a C 1s position of 284.7 eV, in agreement with literature values for ubiquitous carbon. [28]

2.4. Catalytic Activity. The catalytic activity measurements were conducted in an experimental setup described previously. [21] The composition of the feed gas was mixed by digital mass flow controllers and a controlled liquid evaporation unit. The gas-phase concentration of CO was 2 vol% (abbreviated as % in the following). The gas stream was always balanced with argon to yield a total flow of 100 mL/min. For a 8% or 10% H_2O concentration in the gas-phase, 0.384 or 0.480 g/h deionized water (electric conductivity < 3 μS m^{-1}) was dosed through the liquid mass flow meter and evaporated into the (CO)/Ar stream by a controlled evaporation mixer. To dose 8% $H_2{}^{18}O$ into the gas stream, 0.422 g/h $H_2{}^{18}O$ (97 %+ ^{18}O, Eurisotop) were evaporated. The gas-phase composition was analyzed quantitatively by Fourier transform infrared spectroscopy (Tensor 20, Bruker, resolution: 4 cm^{-1}) by measuring a spectrum as an average of 125 scans every minute. A >6-point calibration for CO_2 (Crystal mixture of 1.020% ± 0.020% CO_2 (99.995%) and N_2 (99.999%), Air Liquide), CO (99.997%, Air Liquide), and H_2O (electric conductivity < 3 μS m^{-1}) in argon (99.996%, Westfalen) allows for direct calculation of the concentration of CO, CO_2, and H_2O from the infrared spectra.

Additional experiments to evidence H_2 evolution were performed using a heatable quartz tubular reactor attached to an online mass spectrometer for gas-phase analysis as described elsewhere. [29] The catalyst (36.7 mg) was filled into the reactor. As gas feed, 2% CO/10% H_2O

balanced with He to yield a total flow rate of 50 ml/min was used. The catalyst temperature varied between 120°C and 200°C.

2.5. Operando Spectroscopy. *Operando* Raman and UV-Vis spectra were measured by using an experimental setup described previously. [21] [28] Raman spectra were recorded on an HL5R transmission spectrometer (Kaiser Optical) using 532 nm laser excitation from a frequency-doubled Nd:YAG laser (Cobolt). The spectral resolution is specified as 5 cm^{-1}, however, the stability of the band positions is better than 0.3 cm^{-1}. A super notch filter allows detection of Raman shifts starting at ~150 cm^{-1}. The laser power at the sample was adjusted to 1 mW to avoid damage caused by the laser beam. *Operando* Raman spectra of the Au/CeO_2 catalyst were corrected by the reflectivity $R_{\infty,532\ nm}$ of the sample as derived from the UV-Vis spectrum following the approach by Kuba et al. [30] For that purpose, a UV-Vis spectrum was measured after each Raman spectrum. UV-Vis spectra were measured in diffuse reflection mode on an AvaSpec-ULS2048 (Avantes) using D_2 and halogen light sources. As the white standard, MgO powder was employed in the same geometry as the sample. The sampling time was 60 s, resulting from a 300 ms exposure time and averaging over 200 spectra. For quantitative gas-phase analysis, a Fourier transform infrared spectrometer (Tensor 20, Bruker, resolution: 4 cm^{-1}) was attached to the exit of the *operando* cell and the effluent gas stream was analyzed by recording infrared gas-phase spectra as described above (see Section 2.4.).

In the following, details on how the *operando* experiments were conducted will be given. The given times refer to Figure 1. The catalyst (25–30 mg in a sample holder 8 mm in diameter and 0.5 mm deep) was first transferred to the reaction chamber and an *ex situ* Raman spectrum was recorded. During the measurement the bypass and the infrared gas cell were cleaned with 100 mL/min argon. Then a background spectrum for the gas-phase analysis was recorded, assuming no residual CO, CO_2, and H_2O in the gas cell. This was confirmed as the spectrum (baseline, no absorption) did not change over time. An argon stream was applied to the reaction chamber

and the sample was heated to 120°C. Residual CO_2 and H_2O desorbed from the sample during heating as seen by the increased CO_2 and H_2O concentration at ~80 min. Two Raman spectra (80 s exposure, 5 accumulations, duration: 26 min each) followed by UV-Vis spectra (300 ms, 200 averages, duration: 1 min) were recorded, while the catalyst was kept in the argon stream at 120°C. Then the gas stream was switched again to the bypass and the sample was kept in a stable inert, argon atmosphere. In the bypass first 2% CO and secondly 8% or 10% water was added to the stream and the mixture was equilibrated for at least 5 min before being applied to the reaction chamber for 1 h. *Dynamic operando* Raman spectra (80 s exposure, 1 accumulation, duration: 80 s each) were taken immediately afterwards for 1 h. Alternatively, steady-state Raman spectra (see above; duration: 26 min) were measured**.**

2.6. Density Functional Theory Calculations. A detailed description of the DFT calculations of ceria model systems and vibrational analysis has been given elsewhere. [22] Briefly, we applied spin-polarized DFT in the DFT+U approach [31] with the generalized gradient–corrected approximation (GGA) of Perdew, Burke and Ernzerhof (PBE). [32] The U_{eff} value of 4.5 eV [33] was used for the Ce 4*f* states. The Kohn–Sham equations were solved employing the projected augmented wave (PAW) method. [34] The Ce (5s, 5p, 6s, 4f, 5d) and O (2s, 2p) valence electrons were treated with a plane wave cutoff of 400 eV. The CeO_2(111) surface was modeled using a supercell containing a three O–Ce–O trilayers (TLs) slab with the CeO_2 bulk equilibrium lattice constant calculated before. [22] (6×6×1) or (3×3×1) Monkhorst–Pack grid sampling [35] was used for surface slabs with (1×1) or (2×2) periodicity, respectively. More than 10 Å of vacuum was added to the slab to avoid interaction between surfaces. The residual force in the structures is 0.01 eV/Å and the self-consistent field (SCF) energy converged to 10^{-6} eV.

In order to calculate the mass-weighted Hessian matrix required for a vibrational frequency calculation in the harmonic approximation, the force-constants were computed by the density functional perturbation (or linear response) theory (DFPT) [36] technique, as implemented in

VASP (the Vienna ab initio simulation package). [37] [38] Raman scattering activity requires computation of the change in the macroscopic dielectric tensor with respect to each normal mode, and thus relates to the third derivative of the energy with respect to atomic positions (see reference [22]). In practice, the dielectric matrix is calculated for two structures where the atoms are displaced by either +0.005 Å or –0.005 Å along each normal mode vector, and derivatives are obtained with a finite differences approach. Successive calculations of Raman activities of normal modes were carried out using a Python script written by Fornari and Stauffer. [39] Infrared absorption intensities were calculated from the effective charge of the ion and the displacement vector. [40] To account for spectral line broadening in the calculated spectra, the intensity of the normal mode was multiplied by a Gaussian function with a 10 cm^{-1} full width at half maximum (FWHM).

3. Results

3.1. Catalyst Characterization. The 0.5 wt% Au/CeO_2 catalyst was characterized by electron microscopy (see Figures S1 and S2) and XPS (see Figure S3), as has been described in detail previously. [21] Briefly, the ceria support consists of 10–15 nm sized crystals. TEM images of the bare ceria support reveal a CeO_2(111) [41] surface termination as well as a stepped surface with corresponding step sites. Scanning TEM (STEM) and TEM images show a small number of gold particles with a size of 10 nm exhibiting characteristic Au(111) peaks. In agreement with the literature, it is proposed that highly dispersed gold particles in direct contact with the ceria support rather than the particles observable with TEM are responsible for the reactivity. [2]

XPS analysis of the 0.5 wt% Au/CeO_2 catalyst revealed two Au 4f components at 84.0 and 84.9 eV, which can be assigned to Au^0 and Au^+, respectively. [22] [27] From quantitative analysis of the surface composition the fraction of Au^+ was determined to be 30%. Analysis of the Ce 3d photoemission revealed a fraction of 15% Ce^{3+} for Au/CeO_2 (see Figure S3) as compared to 13% Ce^{3+} for the bare support. This behavior suggests a charge transfer from gold to the ceria support as proposed by DFT+U calculations of gold adsorption on the oxidized CeO_2(111) surface. [42] [43]

3.2. Catalytic Activity. Figure 1 demonstrates the activity of the 0.5 wt% Au/CeO_2 catalyst for WGS reaction at 120°C. The gas-phase composition as determined by infrared gas-phase spectroscopy is shown for varying gas feed compositions at 120°C. This setup was also employed for the *operando* experiments described below (see Section 3.4.). The catalytic activity is measured as vol% CO_2 determined by FTIR analysis at the outlet of the reaction cell divided by vol% CO applied, corresponding to the conversion of CO to CO_2. The conversion (%) is shown in black, the CO concentration (%) in red, and the H_2O concentration (%) in blue. After initial exposure to pure argon (starting after ~80 min), the reaction gas mixture (2% CO,

8% H_2O) was equilibrated in the bypass (at ~155 min) and subsequently applied to the reaction chamber (starting after ~170 min), resulting in catalytic activity as indicated by the rise in CO_2 concentration. The catalyst exhibited a steady-state activity of 3.5% as determined by the CO_2 content in the gas stream. After 230 min, the catalyst was exposed to 8% H_2O and cooled down to room temperature in argon. Finally, the cell was cleaned from water in pure argon. Note that the empty reaction cell did not exhibit any CO_2 evolution in the same CO/H_2O mixture up to 175°C.

The evolution of H_2, which is not accessible by infrared spectroscopy, was demonstrated in a quartz tubular reactor attached to an online mass spectrometer. At 50 mL/min total flow and 2% CO, 10% H_2O in He, the measured H_2 concentration is identical to the CO_2 concentration in the product stream for sample temperatures between 120°C and 200°C (not shown), while the corresponding bare ceria support was inactive. The activation energy is determined to be 46.2 ± 0.9 kJ/mol between 120 and 200°C (see Figure S4), which is in line with the reported value of 47.8 ± 1.5 kJ/mol for 0.44 wt% Au/$CeLaO_x$ (8% La) catalyst where metallic gold was leached from the samples with cyanide. [2] [44]

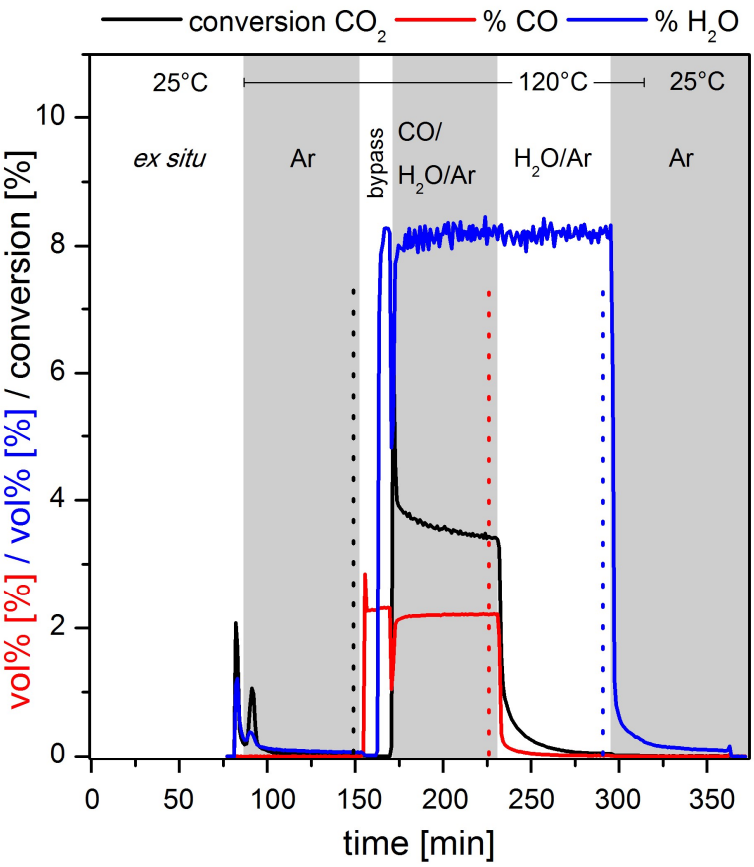

Figure 1. Gas-phase analysis by infrared spectroscopy over a 0.5 wt% Au/CeO_2 catalyst for varying feed compositions. The conversion (%) of CO to CO_2 is shown in black, the CO concentration (%) in red and the H_2O concentration (%) in blue. The reaction gas mixture (2% CO, 8% H_2O) is equilibrated in a bypass and subsequently applied to the reaction chamber at a catalyst temperature of 120°C and at a total flow rate of 100 mL/min. The catalyst is regenerated in 8% H_2O and cooled down to 25°C in argon. In the case of *operando* experiments the dashed lines indicate the end of the Raman measurements.

3.3. *Operando* Raman Spectroscopy. Figure 2 depicts *operando* Raman spectra of a 0.5 wt% Au/CeO_2 catalyst at 120°C in argon atmosphere during WGS reaction (2% CO, 8% H_2O), and in H_2O (8%) showing the phonon (0–1000 cm^{-1}, left panel) and adsorbate (800–2300 cm^{-1}, right panel) regions, respectively. The end of each measurement is indicated by the dashed lines in Figure 1. The position of the most intense band (F_{2g} mode) is given at the top left of Figure 2. In Argon flow, the F_{2g} band is located at 459.5 cm^{-1} showing a significant redshift (~4 cm^{-1}) as compared to spectra measured at room temperature. [21] [24] In addition the F_{2g} band position is redshifted by ~2 cm^{-1} as compared to the bare CeO_2 support. For example, the position of the F_{2g} band of bare ceria in argon atmosphere at 120°C is 461.7 cm^{-1} (see Figure S7). We take the latter F_{2g} band position as a reference state for CeO_{2-x}, where x accounts for intrinsic oxygen defects in ceria. With respect to this F_{2g} band position the stoichiometry of Au/CeO_2 in argon is determined to be $CeO_{1.947-x}$, and under WGS reaction conditions, as $CeO_{1.873-x}$ (corresponding to an F_{2g} position of 456.4 cm^{-1}), based on the shift of the F_{2g} band. For details about the derivation of the relationship between the redshift of the F_{2g} band position and the stoichiometry of ceria from DFT+U results please refer to the literature. [21] Almost the same F_{2g} position as in argon atmosphere is observed in water atmosphere after exposure to reaction conditions (459.3 cm^{-1}). Obviously, the reduction of the Au/CeO_2 catalyst under reaction conditions is reversible, underlining the importance of *operando* experiments to elucidate the active state of the catalyst. An increased concentration of oxygen vacancies in the subsurface region of the ceria support under reaction conditions is also indicated by the broad increase of the defect bands at 540 and 560 cm^{-1}, as can be seen in the left panel of Figure 2. As discussed previously on the basis of DFT+U calculations, [22] these bands can be assigned to a $Ce^{3+}O_8$ coordination cube (oxygen vacancy in the second coordination sphere of Ce^{3+}) and to a $Ce^{3+}O_7V_O^{\bullet\bullet}$ coordination cube (oxygen vacancy in the direct proximity of Ce^{3+}), respectively. Qualitatively, the increased intensity of the 560 cm^{-1} band indicates a higher concentration of oxygen vacancies, because the oxygen defect and Ce^{3+} cannot avoid each other in the ceria

lattice at higher concentrations of oxygen vacancies. The concentration is quantified by the F_{2g} position using DFT+U calculations as described above. [22]

The longitudinal and transversal stretching modes of the CeO_2(111) surface are observed at 242 and 402 cm^{-1}. [22] The longitudinal surface mode is redshifted by 4 cm^{-1} at 120°C compared to room temperature measurements. [21] Interestingly, both bands disappear during WGS reaction, while their intensities in water atmosphere are very similar to those measured in argon. Obviously, also the surface processes at the Au/CeO_2 catalyst are reversible in H_2O. As shown in the right panel of Figure 2, the adsorbate region is characterized by Raman bands at 1250, 1375, 1590, 1650, and 1872 cm^{-1}, besides the ceria 2LO overtone at 1170 cm^{-1} [22]. Please note that the 1250 cm^{-1} band is covered by the 2LO overtone. The bands at 1250, 1375, and 1590 cm^{-1} are assigned to formate species adsorbed at the ceria surface, whereas the band at 1650 cm^{-1} is attributed to hydrogen carbonate species. For an unambiguous identification of carbonate, hydrogen carbonate, and formate in the experimental spectra, these species were modeled at the CeO_2(111) surface (see Figure S6). The results of the DFT+U calculations for carbonate [45] [46] hydrogen carbonate, [45] and formate species [47] are summarized in Table 1. The results are in agreement with those reported in the literature.

For comparison, for bare ceria one observes no shift of the F_{2g} band position, no defect band increase, and no formate-related bands under WGS reaction conditions. Besides, the surface modes at 246 and 402 cm^{-1} do not show any intensity changes at the bare ceria support (see Figures S7 and S8 for Raman spectra during exposure to CO/$H_2{}^{18}O$, which are identical to those measured in CO/$H_2{}^{16}O$).

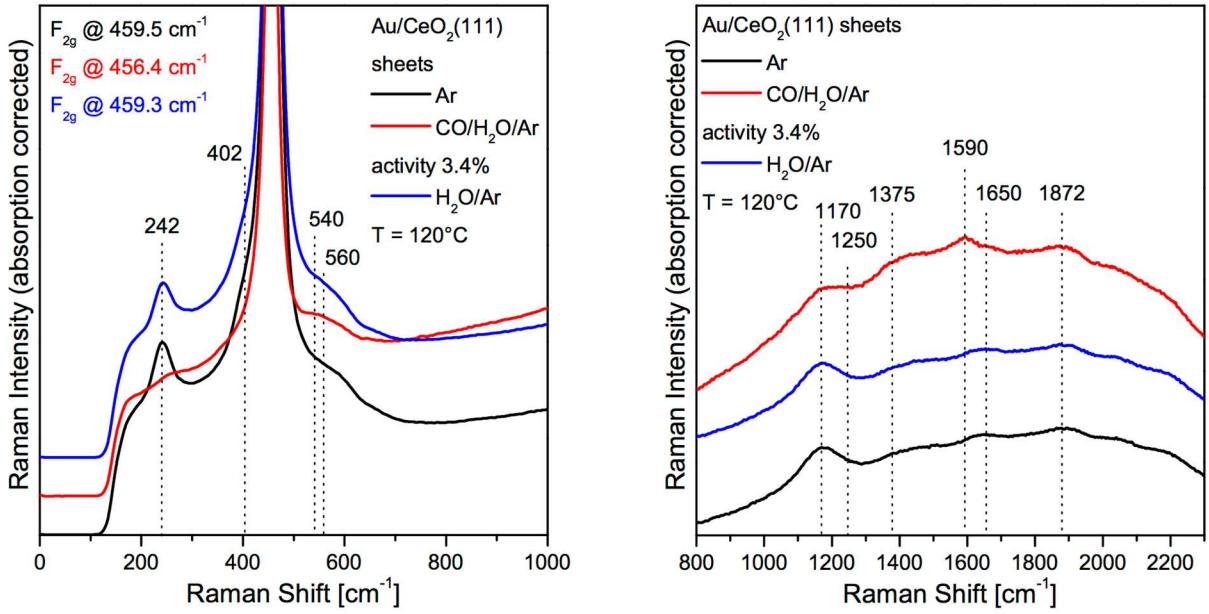

Figure 2. *Operando* Raman spectra of 0.5 wt% Au/CeO_2 at 120°C during WGS reaction (2% CO, 8% H_2O, red) showing the phonon (left) and adsorbate (right) regions. For comparison spectra in argon prior to reaction (black) and in 8% H_2O after reaction (blue) are shown. As the F_{2g} band is cut off, the F_{2g} band positions are given at the top left. Spectra are offset for clarity.

Table 1. Experimental and calculated Raman properties of carbonate, hydrogen carbonate, and formate species at the $CeO_2(111)$ surface. The region printed in bold refers to the maximum and minimum wavenumber values of the corresponding vibration based on all different configurations. For the formate species, Raman properties of $CH^{16}O$ and $CH^{18}O$ adsorbed at the $Ce^{18}O_2(111)$ surface are also included. (s) and (as) refer to symmetric and asymmetric stretching modes, respectively. O_{out} and O_{lat} refer to larger vibrational amplitudes of the outer oxygen or the oxygen at the lattice position, respectively. The structures and configurations are described in Table S2, and Figure S6 depicts the most stable configurations.

Structure	**DFT+U**			**Experiment**		**Assignment**
	Frequency/Region	**Intensity**		**Frequency**		
		IR	**Raman**	**IR**	**Raman**	
	[cm^{-1}]	**[%]**	**$Å^2$ $u^{1/2}$**	**[cm^{-1}]**	**[cm^{-1}]**	
CO_2 gas	2358	100	-	2349		ν(CO_2) (as)
	1316					ν(CO_2) (s)
	633					δ(CO_2)
Carbonate	1592	100	119	1575		ν(CO_2) (as)
	1239	27	127	1298		ν(CO_2) (s)
	949	27	262	988		ν($CO_{lattice}$)
Hydrogen	3667 / **3659-3672**	9	339	3619		ν(OH)
carbonate	1608 / **1608-1655**	100	73	1620	1650	ν(OCO, as)
	1395 / **1336-1395**	41	37	1393		ν(OCO, s)
	1178 / **1170-1181**	30	10	1218		δ(OCOH)
	1007 / **999-1008**	4	25	1023		ν(CO_3, s)
Formate	2931 / **2930-2937**	7	262	2937		ν(CH)
$^{12}CH^{16}O_{out}$/	1580 / **1580-1602**	87	94	1549	1590	ν(OCO, as, O_{out})
$Ce^{16}O_2$(111)	1340 / **1338-1340**	2	27	1358	1375	ν(OCO, s)
($^{16}O_{lat}$)	1283 / **1253-1283**	29	45	1254	1250	ν(OCO, as, O_{lat})
	1020 / **1017-1020**	0	52	1050	-	δ(HCOO)
Formate	2931	7	262			ν(CH)
$^{12}CH^{16}O_{out}$/	1579	87	94		1590	ν($^{16}OC^{18}O$, as, O_{out})
$Ce^{18}O_2$(111)	1339	2	27		1375	ν($^{16}OC^{18}O$, s)
($^{18}O_{lat}$)	1253	29	45		1220	ν($^{16}OC^{18}O$, as, O_{lat})
	1018	0	52		-	δ(HCOO)
Formate	2931	7	262			ν(CH)
$^{12}CH^{18}O_{out}$/	1552	87	94		-	ν($^{18}OC^{18}O$, as, O_{out})
$Ce^{18}O_2$(111)	1330	2	27		-	ν($^{18}OC^{18}O$, s)
($^{18}O_{lat}$)	1249	29	45		-	ν($^{18}OC^{18}O$, as, O_{lat})
	1017	0	52		-	δ(HCOO)

3.4. *Operando* Raman Spectroscopy using $H^{18}O$. To gain insight into the mechanism of the WGS reaction over Au/CeO_2 catalysts, *operando* Raman spectra were measured during exposure of the catalyst to 2% CO/8% $H_2{}^{18}O$. As water activation and O-H bond cleavage have been proposed as rate determining steps for the WGS reaction, the replacement of ^{16}O by ^{18}O is expected to provide fundamental new insight into the reaction mechanism over Au/CeO_2 catalysts, especially as the vibrational properties of the ceria support are altered by ^{18}O incorporation and can be probed by *operando* Raman spectroscopy, as described below. Analysis of the gas-phase composition during $CO/H_2{}^{18}O$ WGS reaction and comparison with literature data for rotational vibrational spectra of $C^{16}O_2$, $C^{18}O_2$, and $C^{16}O^{18}O$ [48] reveals that the product gas stream consists of $C^{16}O^{18}O$ after an initial short period (<3 min), in which both $C^{16}O_2$ and $C^{16}O^{18}O$ are detected simultaneously. As no separate calibration for the $C^{16}O^{18}O$ concentration was done, the activity of the catalyst was estimated to be 3–4% based on $C^{16}O_2$, which is comparable to the activities obtained for experiments with $H_2{}^{16}O$. It is expected that the ^{18}O isotope has only minor influence on the activity (negligible kinetic isotope effect of the chemical reaction).

Figure 3 depicts *operando* Raman spectra of a 0.5 wt% Au/CeO_2 catalyst at 120°C during WGS reaction with $H_2{}^{18}O$ (2% CO, 8% $H_2{}^{18}O$, orange) together with spectra in argon prior reaction (black) and in 8% $H_2{}^{18}O$ after reaction (dark blue) for comparison. At first sight, the *operando* Raman spectra in Figure 3 resemble those obtained for the $H_2{}^{16}O$ isotope, i.e., the longitudinal and transversal modes of the $CeO_2(111)$ surface disappear and the defect bands at 540 and 560 cm^{-1} increase in intensity. Interestingly, the F_{2g} band maximum is located at 440.4 cm^{-1}, as compared to 456.4 cm^{-1} for the reaction with $H_2{}^{16}O$. This behavior can be rationalized by considering the band at 440.4 cm^{-1} to consist of two components representing F_{2g} modes in $Ce^{18}O_2$ and in $Ce^{16}O_2$. This demonstrates that ^{16}O of the support in gold/ceria catalyst is readily exchanged with ^{18}O from $H_2{}^{18}O$ under reaction conditions.

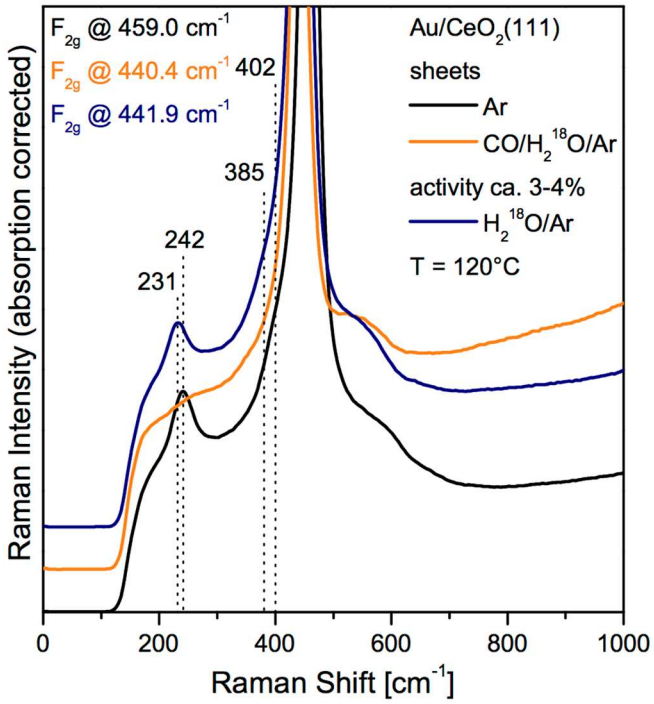

Figure 3. *Operando* Raman spectrum of 0.5 wt% Au/CeO_2 at 120°C during WGS reaction (2% CO, 8% $H_2{}^{18}O$, orange). For comparison spectra in argon prior to reaction (black) and in 8% $H_2{}^{18}O$ after reaction (dark blue) are shown. Because the F_{2g} band is cut off the positions of the F_{2g} band are given at the top left. Spectra are offset for clarity.

We modeled the $Ce^{18}O_2(111)$ surface to evaluate the effect of isotopic exchange (^{16}O ➔ ^{18}O) of surface and bulk oxygen on the position of the surface modes and the F_{2g} mode shifts. The results of the DFT+U calculations of the Raman spectrum of the $Ce^{18}O_2(111)$ surface are shown in Figure 4. For the surface modes, 11 and 17 cm^{-1} redshifts are calculated for the longitudinal and transversal surface modes, respectively, while a 24 cm^{-1} shift is calculated for the F_{2g} mode. The surface and bulk phonons can likewise be treated as isolated vibrations of $^{140}Ce^{16/18}O$ oscillators (see Supporting Information). The shift attributed to the isotope exchange is then

calculated from its reduced masses as $\nu(^{140}Ce^{18}O) = 0.9488 \cdot \nu(^{140}Ce^{16}O)$, corresponding to a 22 cm^{-1} redshift of the F_{2g} band for a $Ce^{18}O_2$ lattice. A detailed discussion of the deconvolution of the $^{16}O/^{18}O$ composite F_{2g} band reveals two components, at 456 and 436 cm^{-1}, and will be presented in the context of the *dynamic operando* Raman spectra (see Section 3.5). This 20 cm^{-1} difference is consistent with the calculated difference for the F_{2g} band positions of $Ce^{16}O_2$ and $Ce^{18}O_2$ lattices, abbreviated as ^{16}O F_{2g} and ^{18}O F_{2g} in the following. In fact, the deconvolution reveals that the majority of the probed sample contains ^{18}O lattice oxygen. Please note, that upon switching from reaction conditions to 8% $H_2{}^{18}O$, the position of the F_{2g} band maximum is almost maintained (see dark blue spectrum in Figure 3).

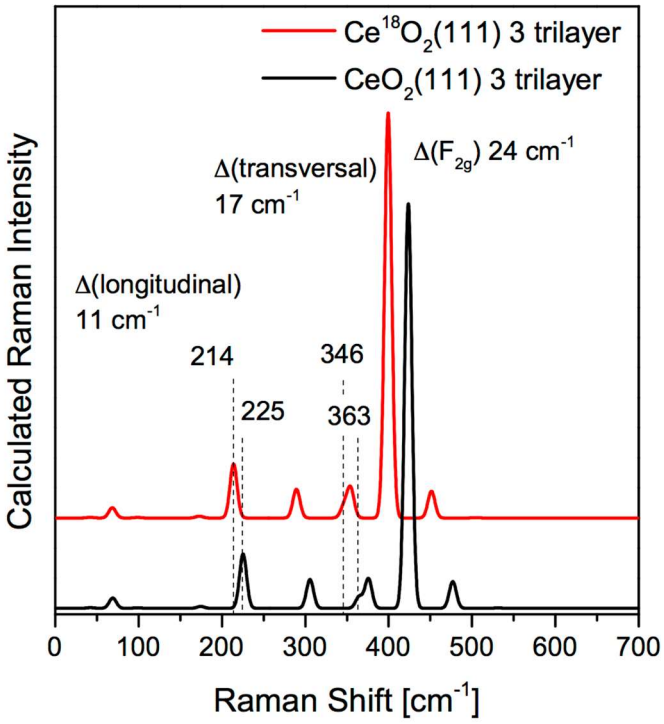

Figure 4: Comparison of the calculated Raman spectra of the $Ce^{16}O_2(111)$ (black line) and $Ce^{18}O_2(111)$ surface (red line). Three O–Ce–O trilayers (TLs) were considered at (1×1) periodicity.

As another interesting aspect of the results, Figure 3 shows that in 8% $H_2{}^{18}O$/Ar after reaction the longitudinal and transversal mode are located at 231 and 385 cm^{-1}, respectively. This corresponds to 11 cm^{-1} and 17 cm^{-1} redshifts, respectively, as compared to the position in argon atmosphere before the reaction. Again, this behavior is in accordance with the redshifts of 11 and 17 cm^{-1} calculated by DFT+U for the $Ce^{18}O_2(111)$ surface and the estimated shifts on the basis of the isolated Ce-$^{16/18}$O oscillator model. As a consequence, we conclude that a complete exchange of the surface oxygen from ^{16}O to ^{18}O occurred at the Au/CeO_2 catalyst during the reaction with $H_2{}^{18}O$ as reactant, in addition to the exchange of subsurface oxygen discussed above.

In comparison, Raman spectra of the bare ceria support recorded in the presence of CO/$H_2{}^{18}O$ or $H_2{}^{18}O$ exhibit neither a shift of neither the F_{2g} band nor the bands assigned to the longitudinal or transversal ceria surface modes (see Figure S7). Furthermore, no formate-related bands at 1375 or 1590 cm^{-1} are observed for bare ceria (see Figure S8). In contrast, the hydroxyl bands at 3653 and 3682 cm^{-1} (see Figure 5, left panel) shift by 10 and 12 cm^{-1} to 3643 and 3670 cm^{-1} at the ceria support, respectively. This behavior coincides well with the estimated isotope factor based on isolated $^{16}O/^{18}O$-^{1}H oscillators of $\sqrt{\frac{16/17}{18/19}} = 0.9967$. On the other hand, the Raman spectrum of bare ceria exposed to CO / $H_2{}^{16}O$ (see Figure 5, right panel) did not show any shifts of the hydroxyl bands confirming the exchange of terminal hydroxyl groups (OH) upon $H_2{}^{18}O$ exposure, whereas lattice oxygen (O^{2-}) in bare ceria is not liable to isotope exchange. Please note that the hydroxyl vibrations of the Au/CeO_2 catalyst could not be evaluated because of strong fluorescence present in this type of samples.

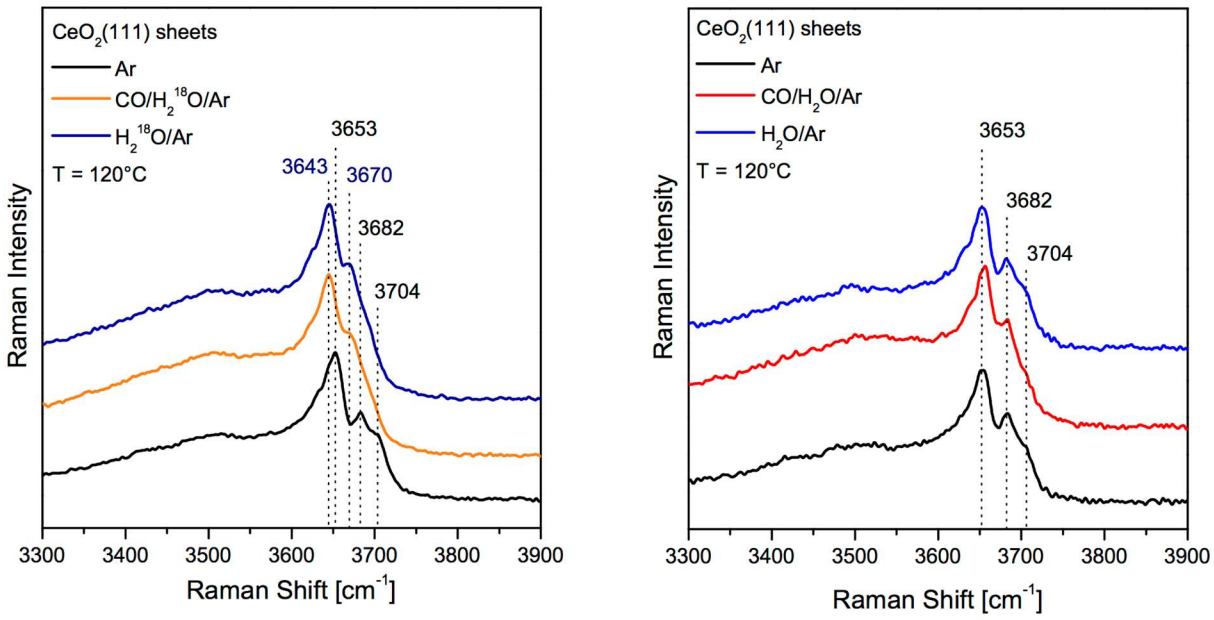

Figure 5: Raman spectra of bare CeO_2 at 120°C during exposure to WGS reaction conditions (left panel: 2% CO, 8% $H_2{}^{18}O$, orange; right panel: 2% CO, 8% $H_2{}^{16}O$, red). For comparison spectra in argon (black), in 8% $H_2{}^{18}O$ (dark blue left panel), and in 8% $H_2{}^{16}O$ (blue right panel) are shown. Spectra are offset for clarity.

In Figure 6, *operando* Raman spectra of the Au/CeO_2 catalyst during WGS reaction are compared to *in situ* Raman spectra in various gas atmospheres. The black spectrum corresponds to the spectrum of the Au/CeO_2 catalyst equilibrated in argon at 120°C as in Figures 2 and 3. Please note that prior to all measurements the catalyst was equilibrated in argon at 120°C. The red and orange spectra measured in $CO/H_2{}^{16}O$ and $CO/H_2{}^{18}O$ have been discussed before. The spectrum in $H_2{}^{16}O/Ar$ (blue) resembles the spectrum in $H_2{}^{16}O/Ar$ after reaction (see Figure 2). Interestingly, upon exposure of the Au/CeO_2 catalyst to $H_2{}^{18}O$ the bands assigned to the longitudinal and transversal surface modes shift to 231 and 385 cm^{-1}, respectively. As discussed above this indicates that all ^{16}O atoms of the $CeO_2(111)$ surface are replaced by ^{18}O atoms. Obviously for a complete isotope exchange of the surface oxygen ions (O^{2-}), exposure to $H_2{}^{18}O$ atmosphere is sufficient. Under these conditions the F_{2g} band position is not shifted indicating that only oxygen ions of the surface layer have been replaced for ^{18}O isotopes.

The Raman spectrum recorded in CO/Ar resembles the spectrum in $CO/H_2{}^{16}O/Ar$, i.e., the bands assigned to the surface modes at 242 and 402 cm^{-1} are absent, and the F_{2g} position and the defect band profile are identical. A similarity of the spectral behavior in CO/Ar and $CO/H_2{}^{16}O/Ar$ was also observed in UV-Vis absorption (see Figure S9). In contrast, for CO oxidation reaction conditions (2% CO, 10% O_2) at 120°C, the $CeO_2(111)$ surface modes are observed with the same intensity as in argon atmosphere, and the F_{2g} band and defect band profile mirror the behavior in argon atmosphere as well. Obviously, surface and subsurface oxygen of the Au/CeO_2 catalyst, withdrawn by CO oxidation in CO atmosphere, [21] are replenished at 120°C if O_2 is available in the gas-phase.

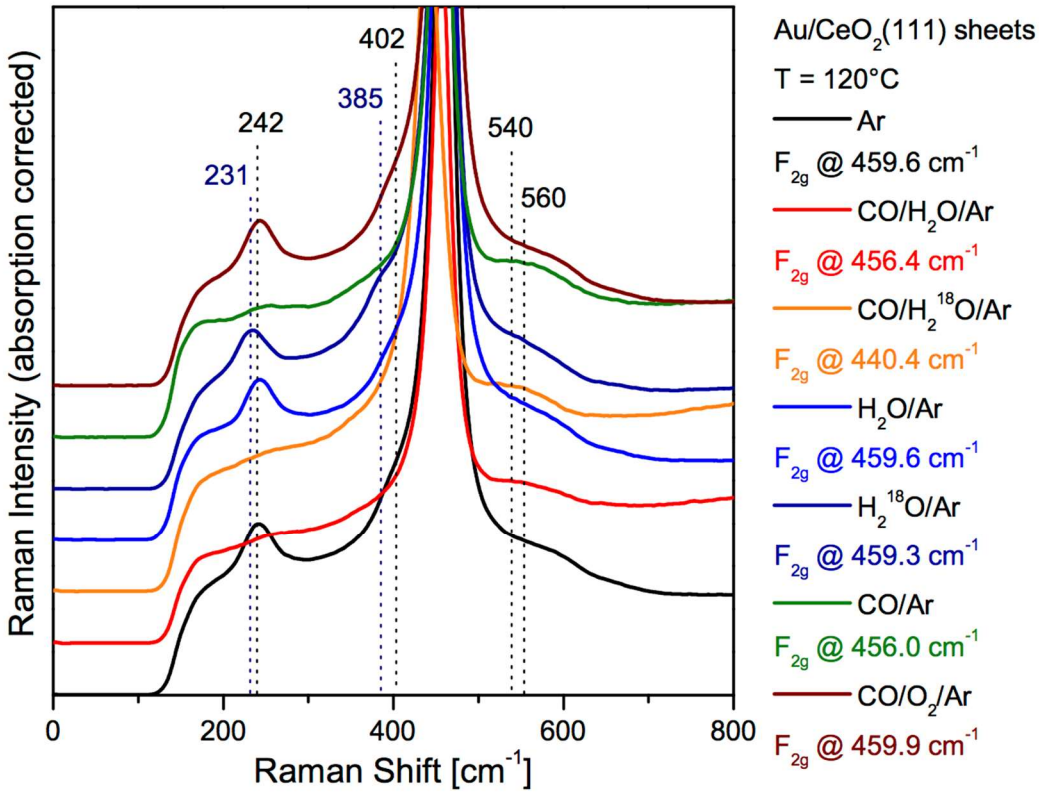

Figure 6. *In situ/operando* Raman spectra (phonon region) of a 0.5 wt% Au/CeO_2 at 120°C exposed to argon (black), WGS reaction conditions (2% CO, 8% $H_2{}^{16}O$, red), WGS reaction conditions (2% CO, 8% $H_2{}^{18}O$, orange), 10% $H_2{}^{16}O$ (blue), 8% $H_2{}^{18}O$, (dark blue), 2% CO (green), and CO oxidation reaction conditions (2% CO, 10% O_2, brown). Prior to all measurements the catalyst was equilibrated in argon at 120°C. The F_{2g} band is cut off and the position of the F_{2g} band is given at the right of the panel. Spectra are offset for clarity.

The absence of the two surface modes can either be explained by the formation of surface oxygen defects as discussed previously [22] or by the formation of hydroxyl groups through adsorption of water in the surface defects. To gain insight into how water adsorption alters the Raman spectrum of CeO_2(111) –terminating ceria nanoparticles [22] we modeled the molecular (MS1) and dissociative (HP1) adsorption of water at the CeO_2(111) surface [49] as well as the dissociative adsorption of water into an oxygen defect at the CeO_{2-x}(111) surface (see Figure S5 for structures). Table S1 summarizes the adsorption energies for the most stable configurations, which are in agreement with the literature values. [49] [50] The calculated Raman spectra for water adsorbed in molecular (MS1) or in dissociated form (HP1) form at the CeO_2(111) surface are shown in Figure 7. The longitudinal surface mode originally observed at 225 cm^{-1} shifts slightly to higher wavenumbers. However, the band completely disappears upon water adsorption into the oxygen defect of a reduced CeO_{2-x}(111) surface and formation of two surface hydroxyl groups (DD2, see Figures S5 D) and E) for corresponding structures), which is predicted to be a highly exothermic process (-2.024 eV, see Table S1).

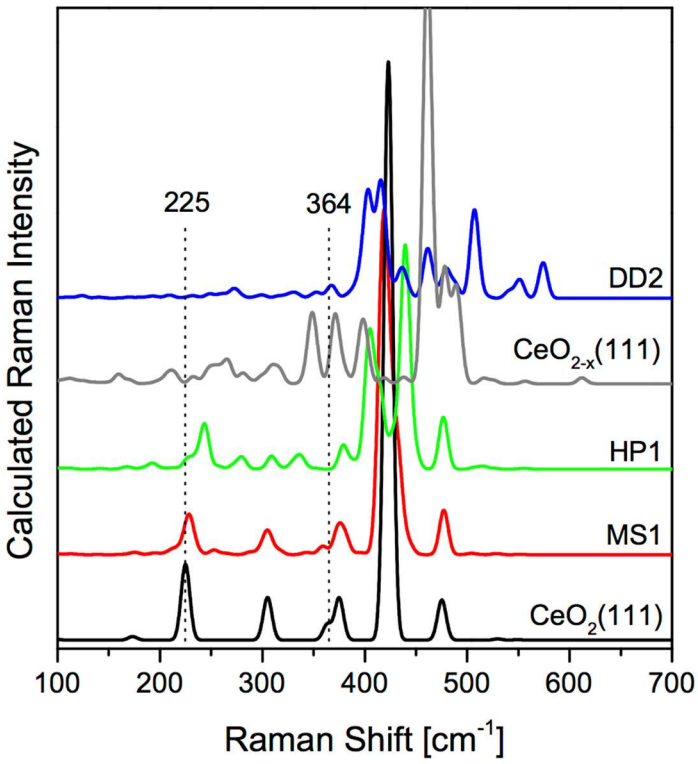

Figure 7: Calculated Raman spectra of molecular (MS1) and hydroxyl pair adsorption (HP1) of H_2O at the oxidized $CeO_2(111)$ surface, the reduced $CeO_{2-x}(111)$ surface and dissociative adsorption of H_2O (DD2) at the $CeO_{2-x}(111)$ surface with (2×2) periodicity.

Figure 8 shows the corresponding adsorbate region of the *in situ/operando* Raman spectra. The measurements were conducted in the same manner as described in the context of Figure 6. The band at 1872 cm^{-1} originates from residual adsorbed water and remains stable under all conditions. Although the catalyst is exposed to $H_2{}^{18}O$ (orange and dark blue spectra) the observed bending mode of adsorbed water is hardly affected by the isotope exchange. This can be rationalized by the small isotope shift of the bending mode in $H_2{}^{18}O$ (ν = 1588.3 cm^{-1} [51]) as compared to $H_2{}^{16}O$ (ν = 1594.7 cm^{-1} [52]) and the rather large bandwidth. The small and broad band due to hydrogen carbonate at 1650 cm^{-1} is observed most clearly in argon atmosphere. Under reaction conditions (CO, $H_2{}^{16}O$) formate species HCOO are formed, as indicated by the bands at 1590 cm^{-1} (DFT+U: 1580 cm^{-1}), 1375 cm^{-1} (DFT+U: 1340 cm^{-1}), and 1250 cm^{-1} (DFT+U: 1283 cm^{-1}). The first band is assigned to an asymmetric stretching mode ν(OCO, as, O_{out}) involving the outer oxygen (O_{out}) of the formate species, the second to the symmetric stretching mode ν(OCO, s), and the third to an asymmetric stretching mode ν(OCO, as, O_{lat}) involving the lattice oxygen (O_{lat}) (see Table 1). Only the latter band is shifted to 1220 cm^{-1} upon exposure to (CO, $H_2{}^{18}O$) suggesting, that the outer oxygen is ^{16}O, while the oxygen at the lattice position (O_{lat}) in $HCO^{18}O_{lat}$ is indeed ^{18}O (see Table 1). Only this formate configuration allows the bands at 1375 and 1590 cm^{-1} to remain almost stable and the band at 1250 to shifts to 1220 cm^{-1} in CO/$H_2{}^{18}O$ atmosphere. Thus, the formate-related bands increase under reaction conditions, while the hydrogen carbonate band remains stable. As the majority component of the F_{2g} phonon redshifts by a factor of 0.9488 due to ^{18}O exchange, the shift of the 2LO overtone by the same factor from 1170 to 1118 cm^{-1} can be rationalized.

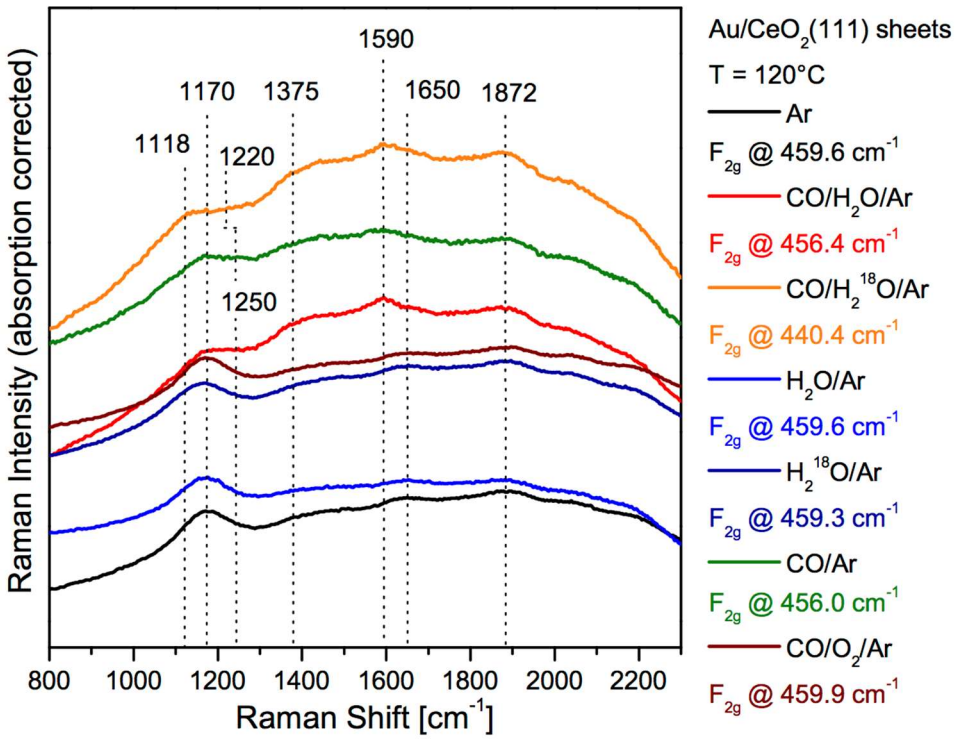

Figure 8. *In situ/operando* Raman spectra (adsorbate region) of a 0.5 wt% Au/CeO_2 at 120°C exposed to argon (black), WGS reaction conditions (2% CO, 8% $H_2{}^{16}O$, red), WGS reaction conditions (2% CO, 8% $H_2{}^{18}O$, orange), 10% $H_2{}^{16}O$ (blue), 8% $H_2{}^{18}O$ (dark blue), 2% CO (green), and CO oxidation reaction conditions (2% CO, 8% O_2, brown). Prior to all *in situ* measurements the catalyst was equilibrated in argon at 120°C. The position of the F_{2g} band is given to the right of the panel. Spectra are offset for clarity.

3.5. *Dynamic Operando* Raman Spectroscopy. As mentioned in the experimental section, *dynamic operando* Raman spectra were measured during the initial exposure of the catalyst to reaction conditions. Figure 9 depicts *dynamic operando* Raman spectra of the Au/$Ce^{16}O_2$ catalyst exposed to WGS reaction conditions (2% CO/ 8% $H_2{}^{18}O$). Raman spectra recorded after 3, 10, and 30 minutes are shown as orange, yellow, and red spectra, respectively. As a reference the Raman spectrum in argon prior to reaction is depicted (black spectrum). A gradual redshift of the maximum of the F_{2g} band from 460 to 440 cm^{-1} is observed. In Raman spectra of the catalyst exposed to CO/Ar or CO/$H_2{}^{16}O$/Ar a redshift of the F_{2g} band to 456 cm^{-1} was observed (see Figures 2 and 6), which has been assigned to an increased concentration of oxygen vacancies in the ceria subsurface. [22] [53] However, changes in the vacancy concentration cannot explain the observed redshift of about 20 cm^{-1} upon exposure to CO/$H_2{}^{18}O$. The redshift rather originates from the formation of subsurface $Ce^{18}O_2$, as discussed above. As a result, a composite F_{2g} band is detected, originating from a ^{16}O F_{2g} and a redshifted ^{18}O F_{2g} contribution. In fact, deconvolution of the composite F_{2g} band by two Lorentz functions (FWHM: 28 cm^{-1}) yields a component located at 436 cm^{-1} (^{18}O F_{2g}) besides the fixed component at 456 cm^{-1} (^{16}O F_{2g}). This corresponds to a difference between ^{16}O F_{2g} and ^{18}O F_{2g} of 20 cm^{-1}, which is in agreement with the difference of 24 cm^{-1} derived from DFT+U calculations (see Figure 4) and the difference of 22 cm^{-1} estimated from isolated ^{140}Ce-$^{16/18}O$ oscillators (see Supporting Information). Exemplarily, the two F_{2g} components of the red spectrum are shown in the left panel of Figure 9 as light grey and dark grey line corresponding to ^{16}O F_{2g} and ^{18}O F_{2g}, respectively.

The right panel of Figure 9 depicts the temporal evolution of the integrated intensity of the two F_{2g} components as well as the 242 cm^{-1} surface mode after exposure to WGS reaction conditions (2% CO/ 8% $H_2{}^{18}O$). The ^{16}O F_{2g} intensity decreases gradually reaching its steady-state intensity after ~30 min, while the ^{18}O F_{2g} intensity increases accordingly. Analysis of the longitudinal surface mode at 242 cm^{-1} over the same time span of ~55 min reveals that the

intensity initially drops to its steady-state intensity. So the descriptors for surface and the subsurface oxygen species change at two different time scales. While the descriptor for the surface, i.e., the 242 cm^{-1} band, changes fast with respect to the timescale of the experiment, the descriptor for the subsurface F_{2g} position changes much more slowly. This behavior resembles the surface and subsurface oxygen dynamics obtained during room temperature CO oxidation of the same material. [20]

The black dashed spectrum in the left panel of Figure 9 was measured at 25°C in Argon after exposing the sample to $CO/H_2{}^{18}O$ at 120°C and then to Argon while cooling to 25°C. Interestingly, the position of the F_{2g} position shifts to the position expected for ^{16}O F_{2g} and a component assigned to ^{18}O F_{2g} is not observed. This behavior can be explained by considering that Raman spectroscopy probes a depth that is limited to the subsurface of the ceria support. In addition, ^{18}O is only introduced into the subsurface of the ceria crystal and equilibrates across the whole crystal after reaction (see also discussion on the probe depth of Raman spectroscopy in the Supporting Information).

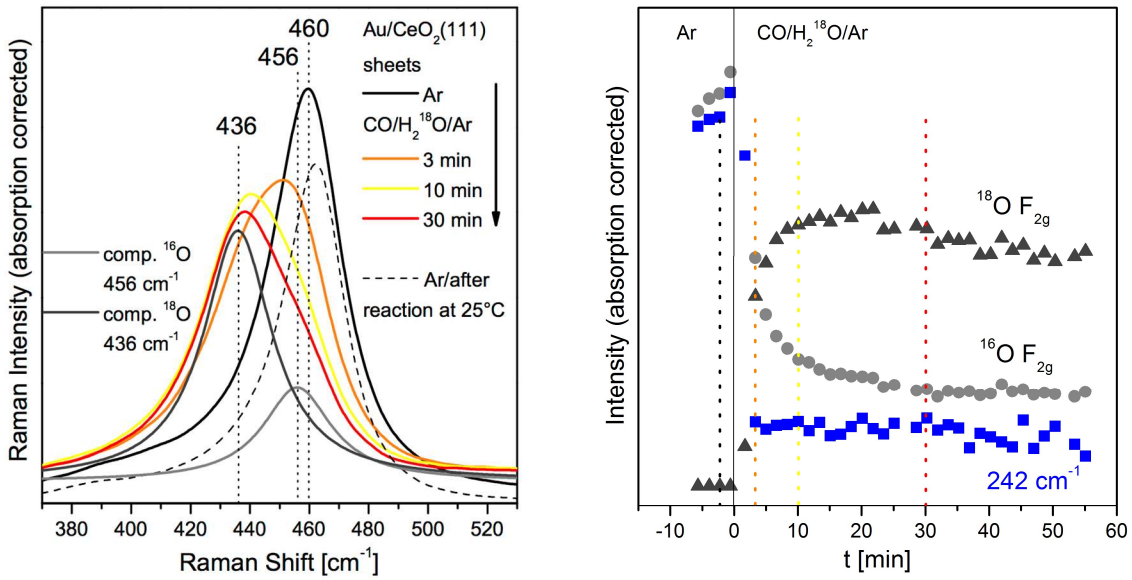

Figure 9. Left panel: *Dynamic operando* Raman spectra of 0.5 wt% Au/CeO_2 at 120°C during WGS reaction conditions (2% CO, 8% $H_2{}^{18}O$). For the spectrum recorded after 30 minutes deconvolution of the F_{2g} mode yields a ^{16}O F_{2g} component at 456 cm^{-1} (light grey) and a ^{18}O F_{2g} component at 436 cm^{-1} (dark grey). The black line corresponds to the spectrum in argon before reaction at 120°C, the dashed line shows the spectrum in argon after reaction at 25°C. Right panel: Temporal evolution of the intensity of the ^{16}O F_{2g} (light grey circles), the ^{18}O F_{2g} (dark grey triangles), as well as the 242 cm^{-1} (blue squares) mode under WGS reaction conditions (2% CO and 8% $H_2{}^{18}O$). Dashed lines indicate the times at which the Raman spectra shown in the left panel were recorded.

4. Discussion

As demonstrated in the results part, Raman spectroscopy provides a way to probe three different type of oxygen species of ceria supported catalysts relevant for WGS reaction conditions, besides the known reduced molecular oxygen species, superoxide (O_2^-) [54] and peroxide (O_2^{2-}). [55] [56] [57]

First, surface hydroxyl groups are probed at the bare ceria support by the O–H stretching mode with frequencies in the range 3643–3704 cm^{-1}. These bands have previously been assigned on the basis of infrared experiments [58] [59] [60] and this assignment will not be further discussed here.

Second, the longitudinal and transversal stretching modes at 242 and 402 cm^{-1} allow the surface oxygen of the CeO_2(111) surface to be probed. Based on DFT+U results, it is proposed that either vacancy formation [22] or hydroxyl formation by water adsorption at a defective CeO_{2-x} surface (see Figure 7) leads to a decrease of the band assigned to the longitudinal stretching mode at 242 cm^{-1}.

And third, the F_{2g} mode provides insight into subsurface oxygen defects [53] [61] and allows a quantification of the oxygen vacancy concentration in the ceria subsurface with the aid of DFT+U calculations. [22] In this context, the defect bands at 540 and 560 cm^{-1} are also of interest, which provide a qualitative interpretation of the oxygen defect concentration in the ceria support.

Besides oxygen species, formate species are observed under reaction conditions, showing characteristic bands at 1250, 1375, and 1590 cm^{-1}. The formate vibrations have previously been observed in infrared experiments. [7] [58] The calculated frequencies and calculated Raman cross sections for formate, carbonate, and hydrogen carbonate species are summarized in Table 1.

As vibrational modes are altered by isotope exchange all the above vibrational modes show a redshift if ^{16}O is replaced by ^{18}O. The shift of solid state and surface phonons was calculated by DFT+U and it turns out that an isolated $^{140}Ce–^{16}/^{18}O$ oscillator model provides an excellent estimate of the isotope shift. Such isolated oscillator calculations were also successfully applied to surface hydroxyl groups, i.e., $^{16}O–H$ and $^{18}O–H$. In addition to the solid state phonon modes, specific vibrational frequencies were calculated for the $^{16}O/^{18}O$ isotopic analogues of formate species (see Table 1).

To gain new insight into the reaction mechanism of the WGS reaction we studied the *operando* Raman spectra upon exposure to $CO/H_2{}^{16}O/Ar$ and $CO/H_2{}^{18}O/Ar$ in great detail. First, the bare ceria support was characterized. Upon exposure to reaction conditions ($CO/H_2{}^{16}O/Ar$) neither catalytic activity nor the formation of formate species is observed. Moreover, terminal hydroxyl groups, and the bulk and surface phonons remain stable in intensity. In the literature, only minor formation of formate species has been proposed for bare ceria on the basis of infrared experiments. [7] Interestingly, upon exposure of the ceria support to $CO/H_2{}^{18}O/Ar$, the terminal hydroxyl groups (O-H) show a redshift indicating an isotope exchange by ^{18}OH for ^{16}OH. Obviously, the hydroxyl groups at the bare ceria support are liable to oxygen exchange at 120°C (see Figure 5), while the lattice oxygen ions (O^{2-}) are not (see Figure S7). For comparison, in a previous study, partial oxygen exchange in polycrystalline ceria by gas-phase O_2 was observed at and above 400°C, consistent with our results. [62]

In the presence of 0.5 wt% Au the behavior of the ceria support changes dramatically. Owing to strong fluorescence the spectral region of the terminal hydroxyl groups is not accessible anymore. On the other hand, exposure to $H_2{}^{18}O/Ar$ results in a complete exchange of surface $^{16}O^{2-}$ ions with $^{18}O^{2-}$ ions as evidenced by the 11 and 17 cm^{-1} shifts of the longitudinal and transversal modes of the $CeO_2(111)$ surface (see Figure 6). Assuming that water adsorbs dissociatively on Au/CeO_2 forming two hydroxyl groups, as has been proposed previously, [63]

formation of ^{18}O surface ions, that are not part of a terminal hydroxyl group, will be accompanied by breaking of two terminal hydroxyl bonds and $H_2{}^{16}O$ formation as shown in Scheme 1.

Previously, based on DFT calculations, O–H bond cleavage has been proposed as the rate determining step of the WGS reaction over Au/CeO_2 catalysts. [12] [20] Our results demonstrate that O–H bond cleavage readily occurs in $H_2{}^{18}O$ atmosphere at 120°C. In fact, as depicted in Figure 6, the whole surface is covered by ^{18}O ions leading to redshifts of 11 and 17 cm^{-1} for the longitudinal and transversal surface modes of the $CeO_2(111)$ surface. Please note that O–H bond cleavage can occur in the absence of CO (see Figure 6 blue and dark blue spectra); thus, for OH bond cleavage during WGS reaction no formation of intermediates such as formate or carboxylate species is required. This is confirmed by our *operando* Raman spectra revealing no variation of formate band intensities under reaction conditions; likewise, no change of carbonate intensities was observed. It should, however, be mentioned that the observation of both formate and carbonate species under reaction conditions is consistent with prior experimental [7] [11] and theoretical [5] [12] studies. The fact that their intensities remain stable strongly indicates their role as spectator species [17] during WGS reaction over Au/CeO_2 catalysts.

Our results show that during exposure of the Au/CeO_2 catalyst to reaction conditions the longitudinal and transversal surface modes are absent. This behavior can be attributed to oxygen vacancy creation or hydroxyl formation at the surface based on DFT+U calculations. As the dissociative adsorption of water into an oxygen vacancy is proposed to be a strongly exothermic process ($E_{\mathrm{ads,H_2O}} = -2.024$ eV, see Supporting Information), [63] it stands to reason that the surface is hydroxylated rather than populated with oxygen vacancies. On the other hand, the F_{2g} band position (456.4 cm^{-1}) strongly suggests an increase in the subsurface oxygen vacancy concentration in $CO/H_2{}^{16}O/Ar$. For comparison, in argon the F_{2g} band is located at 459.5 cm^{-1}

(see Figure 2). The corresponding stoichiometries of the ceria support are $CeO_{1.947-x}$ in argon and $CeO_{1.873-x}$ in reaction atmosphere, thus indicating a strongly reduced ceria subsurface. The reduced state of the catalyst may facilitate O–H bond cleavage, but we have no direct experimental evidence for such a relationship. In any case, based on our Raman spectroscopic evidence for O–H dissociation, we propose as the steps following O–H bond cleavage the transfer of the H atom to the gold particle and the subsequent combination of two H atoms. The latter step has previously been proposed by DFT calculations. [12] Please note that such a reaction pathway does not require the formation of a formate or carboxylate intermediate. Summarizing, while our results are fully consistent with a redox-type mechanism, other reaction mechanisms cannot be ruled out.

The presence of large amounts of ^{18}O in the subsurface in $CO/H_2{}^{18}O/Ar$, as probed by the ^{18}O F_{2g} band at 436 cm^{-1} (see Figure 9), highlights the oxygen dynamics of the ceria support and can be rationalized by a fraction of oxygen vacancies in the subsurface allowing for oxygen ion mobility and transfer of ^{18}O from the surface, i.e., from the adsorption site, to the ceria subsurface. The exchange of ^{18}O to the subsurface happens at a slower timescale than the adsorption and exchange at the surface (see Figure 9).

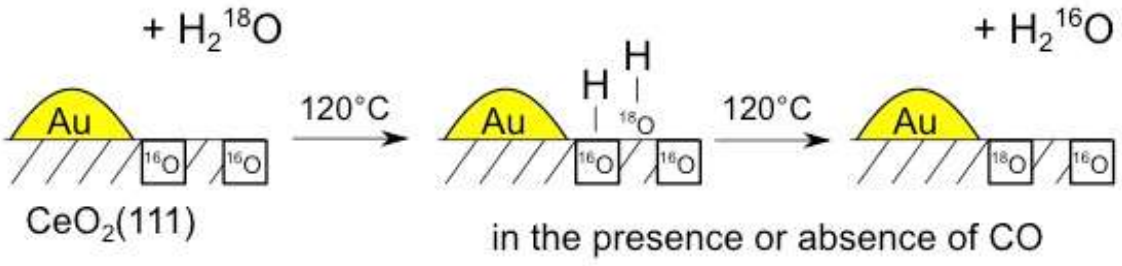

Scheme 1: Reaction scheme for isotopic exchange of ^{18}O from $H_2{}^{18}O$ into a $Ce^{16}O_2(111)$ surface of a Au/CeO_2 catalyst.

5. Conclusions

In a mechanistic study, we explored the potential of *operando* Raman spectroscopy to monitor different surface and bulk oxygen species in a ceria supported gold catalyst (Au/CeO_2) during WGS conditions. With the aid of isotopically labeled water molecules ($H_2{}^{18}O$) and additional DFT+U calculations, fundamental new insight into the reaction mechanism was possible. In particular, the following key results were obtained:

i) The ceria support of a 0.5 wt% Au/CeO_2 catalyst is strongly reduced during WGS conditions and is characterized by extensive oxygen dynamics. Also subsurface oxygen ions are exchanged with gas phase $H_2{}^{18}O$ at 120°C.

ii) Terminal hydroxyl groups (O–H) are volatile to isotopic exchange at the bare ceria support but surface and bulk lattice oxygen ions (O^{2-}) are not.

iii) The modification of ceria with gold allows isotopic exchange of lattice oxygen ions (O^{2-}) of the $CeO_2(111)$ surface even in the absence of CO. The exchange of lattice ions implies twofold O–H dissociation.

iv) During reaction conditions over ceria–supported gold, the ceria surface is hydroxylated. O–H dissociation is proposed to lead to transfer of H atoms to the gold particle and subsequent formation of H_2 by recombination of H atoms.

Summarizing, we provide *operando* spectroscopic data addressing especially the role of the ceria support material to propose a redox-type reaction mechanism for ceria-supported gold catalysts during WGS reaction, while associate mechanisms cannot be ruled out with certainty.

Supporting Information

The Supporting Information cover additional characterization data, operando Raman and UV-Vis spectra, and DFT results, as well as details on the experimental and computational procedures.

Acknowledgments

C. S. gratefully acknowledges the Merck'sche Gesellschaft für Kunst und Wissenschaft e.V. for providing a scholarship. The authors would like to thank M. Verónica Ganduglia-Pirovano and Pablo G. Lustemberg (ICP, Madrid) for support with the DFT calculations, Stefan Knoche (TU Darmstadt) for activity experiments, Stefan Lauterbach and Hans-Joachim Kleebe (TU Darmstadt) for TEM measurements, as well as Karl Kopp for technical support. The calculations were conducted on the Lichtenberg high performance computer of the TU Darmstadt.

References

[1] Ratnasamy, C.; Wagner, J. P. Water Gas Shift Catalysis. *Catal. Rev.* **2009**, *51*, 325-440.

[2] Fu, Q.; Saltsburg, H.; Flytzani-Stephanopoulos, M. Active Nonmetallic Au and Pt Species on Ceria-Based Water-Gas Shift Catalysts. *Science* **2003**, *301*, 935-938.

[3] Jacobs, G.; Chenu, E.; Patterson, P. M.; Williams, L.; Sparks, D.; Thomas, G.; Davis, B. H. Water-Gas Shift: Comparative Screening of Metal Promoters for Metal/Ceria Systems and Role of the Metal. *Appl. Catal. A* **2004**, *258*, 203-214.

[4] Aranifard, S.; Ammal, S. C.; Heyden, A. On the Importance of Metal–Oxide Interface Sites for the Water–Gas Shift Reaction over Pt/CeO_2 Catalysts. *J. Catal.* **2014**, *309*, 314-324.

[5] Chen, Y.; Cheng, J.; Hu, P.; Wang, H. F. Examining the Redox and Formate Mechanisms for Water–Gas Shift Reaction on Au/CeO_2 Using Density Functional Theory. *Surf. Sci.* **2008**, *602*, 2828-2834.

[6] Shido, T.; Iwasawa, Y. Regulation of Reaction Intermediate by Reactant in the Water-Gas Shift Reaction on CeO_2, in Relation to Reactant-Promoted Mechanism. *J. Catal.* **1992**, *136*, 493-503.

[7] Leppelt, R.; Schumacher, B.; Plzak, V.; Kinne, M.; Behm, R. J. Kinetics and Mechanism of the Low-Temperature Water–Gas Shif Reaction on Au/CeO_2 Catalysts in an Idealized Reaction Atmosphere. *J. Catal.* **2006**, *244*, 137-152.

[8] Kalamaras, C. M.; Dionysiou, D. D.; Efstathiou, A. M. Mechanistic Studies of the Water–Gas Shift Reaction over Pt/$Ce_xZr_{1-x}O_2$ Catalysts: The Effect of Pt Particle Size and Zr Dopant. *ACS Catal.* **2012**, *2*, 2729-274

[9] Goguet, A.; Meunier, F. C.; Tibiletti, D.; Breen, J. P.; Burch, R. Spectrokinetic Investigation of Reverse Water-Gas-Shift Reaction Intermediates over a Pt/CeO_2 Catalyst. *J. Phys. Chem. B* **2004**, *108*, 20240-20246.

[10] Meunier, F. C.; Tibiletti, D.; Goguet, A.; Reid, D.; Burch, R. On the reactivity of carbonate species on a Pt/CeO_2 catalyst under various reaction atmospheres: Application of the isotopic exchange technique. *Appl. Catal. A* **2005**, *289*, 104-112.

[11] Mudiyanselage, K.; Senanayake, S. D.; Feria, L.; Kundu, S.; Baber, A. E.; Graciani, J.; Vidal, A. B.; Agnoli, S.; Evans, J.; Chang, R.; Axnanda, S.; Liu, Z.; Sanz, J. F.; Liu, P.; Rodriguez, J. A.; Stacchiola, D. J. Importance of the Metal–Oxide Interface in Catalysis: In Situ Studies of the Water–Gas Shift Reaction by Ambient-Pressure X-ray Photoelectron Spectroscopy. *Angew. Chem. Int. Ed.* **2013**, *52*, 5101-5105.

[12] Chen, Y.; Wang, H.; Burch, R.; Hardacre, C.; Hu, P. New Insight Into Mechanisms in Water-Gas-Shift Reaction on Au/CeO_2(111): A Density Functional Theory and Kinetic Study. *Faraday Disc.* **2011**, *152*, 121-133.

[13] Vecchietti, J.; Bonivardi, A.; Xu, W.; Stacchiola, D.; Delgado, J. J.; Calatayud, M.; Collins, S. E. Understanding the Role of Oxygen Vacancies in the Water Gas Shift Reaction on Ceria-Supported Platinum Catalysts. *ACS Catal.* **2014**, *4*, 2088-2096.

[14] Liu, Z.-P.; Jenkins, S. J.; King, D. A. Origin and Activity of Oxidized Gold in Water-Gas-Shift Catalysis. *Phys. Rev. Lett.* **2005**, *94*, 196102.

[15] Bunluesin, T.; Gorte, R. J.; Graham, G. W. Studies of the Water-Gas-Shift Reaction on Ceria-Supported Pt, Pd, and Rh: Implications for Oxygen-Storage Properties. *Appl. Catal. B* **1998**, *15*, 107-114.

[16] Shido, T.; Iwasawa, Y. Reactant-Promoted Reaction Mechanism for Water-Gas Shift Reaction on Rh-Doped CeO_2. *J. Catal.* **1993**, *141*, 71-81.

[17] Burch, R.; Goguet, A.; Meunier, F. C. A Critical Analysis of the Experimental Evidence for and against a Formate Mechanism for High Activity Water-Gas Shift Catalysts. *Appl. Catal. A* **2011**, *409–410*, 3-12.

[18] Fonseca, A. A.; Fisher, J. M.; Ozkaya, D.; Shannon, M. D.; Thompsett, D. Ceria-Zirconia Supported Au as Highly Active Low Temperature Water-Gas Shift Catalysts. *Top. Catal.* **2007**, *44*, 223-235.

[19] Rodriguez, J. A.; Liu, P.; Hrbek, J.; Evans, J.; Pérez, M. Water gas shift reaction on Cu and Au Nanoparticles Supported on CeO_2(111) and ZnO(0001): Intrinsic Activity and Importance of Support Interactions. *Angew. Chem. Int. Ed.* **2007**, *46*, 1329-1332.

[20] Paier, J.; Penschke, C.; Sauer, J. Oxygen Defects and Surface Chemistry of Ceria: Quantum Chemical Studies Compared to Experiment. *Chem. Rev.* **2013**, *113*, 3949-3985.

[21] Schilling, C.; Hess, C. Real-Time Observation of the Defect Dynamics in Working Au/CeO_2 Catalysts by Combined Operando Raman/UV-Vis Spectroscopy. *J. Phys. Chem. C* **2018**, *122*, 2909-2917.

[22] Schilling, C.; Hofmann, A.; Hess, C.; Ganduglia-Pirovano, M. V. Raman Spectra of Polycrystalline CeO_2: A Density Functional Theory Study. *J. Phys. Chem. C* **2017**, *121*, 20834-20849.

[23] Schilling, C.; Hess, C. CO Oxidation on Ceria Supported Gold Catalysts Studied by Combined Operando Raman/UV–Vis and IR Spectroscopy. *Top. Catal.* **2017**, *60*, 131-140.

[24] Filtschew, A.; Hofmann, K.; Hess, C. Ceria and Its Defect Structure: New Insights from a Combined Spectroscopic Approach. *J. Phys. Chem. C* **2016**, *120*, 6694-6703.

[25] Haruta, M.; Tsubota, S.; Kobayashi, T.; Kageyama, H.; Genet, M. J.; Delmon, B. Low-Temperature Oxidation of CO over Gold Supported on TiO_2, α-Fe_2O_3, and Co_3O_4. *J. Catal.* **1993**, *144*, 175-192.

[26] Pillai, U. R.; Deevi, S. Highly Active Gold-Ceria Catalyst for the Room Temperature Oxidation of Carbon Monoxide. *Appl. Catal. A* **2006**, *299*, 266-273.

[27] Moulder, J. F.; Stickle, W. F.; Sobol, P. E.; Bomben, K. D. *Handbook of X-ray photoelectron spectroscopy. Vol. 40*, Perkin Elmer Eden Prairie, MN, **1992**.

[28] Nottbohm, C. T.; Hess, C. Investigation of Ceria by Combined Raman, UV-Vis and X-Ray Photoelectron Spectroscopy. *Catal. Commun.* **2012**, *22*, 39-42.

[29] Drochner, A.; Ohlig, D.; Knoche, S.; Gora, N.; Heid, M.; Menning, N.; Petzold, T.; Vogel, H. Activity Hysteresis during Cyclic Temperature-Programmed Reactions in the Partial Oxidation of Acrolein to Acrylic Acid. *Top. Catal.* **2016**, *59*, 1518-1532.

[30] Kuba, S.; Knözinger, H. Time-Resolved *In Situ* Raman Spectroscopy of Working Catalysts: Sulfated and Tungstated Zirconia. *J. Raman Spectrosc.* **2002**, *33*, 325-332.

[31] Dudarev, S. L.; Botton, G. A.; Savrasov, S. Y.; Humphreys, C. J.; Sutton, A. P. Electron-Energy-Loss Spectra and the Structural Stability of Nickel Oxide: An LSDA+U Study. *Phys. Rev. B* **1998**, *57*, 1505-1509.

[32] Perdew, J. P.; Burke, K.; Ernzerhof, M. Generalized Gradient Approximation Made Simple. *Phys. Rev. Lett.* **1996**, *77*, 3865-3868.

[33] Fabris, S.; de Gironcoli, S.; Baroni, S.; Vicario, G.; Balducci, G. Taming Multiple Valency with Density Functionals: A Case Study of Defective Ceria. *Phys. Rev. B* **2005**, *71*, 041102.

[34] Blöchl, P. E. Projector augmented-wave method. *Phys. Rev. B* **1994**, *50*, 17953-17979.

[35] Monkhorst, H. J.; Pack, J. D. Special points for Brillouin-zone integrations. *Phys. Rev. B* **1976**, *13*, 5188-5192.

[36] Baroni, S.; de Gironcoli, S.; Dal Corso, A.; Giannozzi, P. Phonons and related crystal properties from density-functional perturbation theory. *Rev. Mod. Phys.* **2001**, *73*, 515-562.

[37] Gajdoš, M.; Hummer, K.; Kresse, G.; Furthmüller, J.; Bechstedt, F. Linear optical properties in the projector-augmented wave methodology. *Phys. Rev. B* **2006**, *73*, 045112.

[38] a) Kresse, G.; Furthmüller, J. Efficiency of Ab-Initio Total Energy Calculations for Metals and Semiconductors Using a Plane-Wave Basis set. *Comput. Mater. Sci.* **1996**, *6*, 15-50. b) Kresse, G.; Furthmüller, J. Efficient Iterative Schemes for *Ab Initio* Total-Energy Calculations Using a Plane-Wave Basis Set. *Phys. Rev. B* **1996**, *54*, 11169-11186. c) Kresse, G.; Hafner, J. Ab Initio Molecular-Dynamics Simulation of the Liquid-Metal–Amorphous-Semiconductor Transition in Germanium. *Phys. Rev. B* **1994**, *49*, 14251-14269. d) Kresse, G.; Hafner, J. Ab Initio Molecular Dynamics for Liquid Metals. *Phys. Rev. B* **1993**, *47*, 558-561.

[39] Fonari, A.; Stauffer, S. *vasp_raman.py*, https://github.com/raman-sc/VASP/, **2013**, accessed on 11/11/2018.

[40] D. Karhánek, *Calculation of vibrational (IR) intensities in VASP 5.**, http://homepage.univie.ac.at/david.karhanek/downloads.html - Entry02, **2012**, accessed on 11/11/2018.

[41] Skorodumova, N. V.; Baudin, M.; Hermansson, K. Surface Properties of CeO_2 from First Principles. *Phys. Rev. B* **2004**, *69*, 075401.

[42] Wang, Y.-G.; Mei, D; Glezakou, V.-A.; Li, J.; Rousseau, R. Dynamic Formation of Single-Atom Catalytic Active Sites on Ceria-Supported Gold Nanoparticles. *Nat. Commun.* **2015**, *6*, 6511.

[43] Camellone, M. F.; Fabris, S. Reaction Mechanisms for the CO Oxidation on Au/CeO_2 Catalysts: Activity of Substitutional Au^{3+}/Au^{+} Cations and Deactivation of Supported Au^{+} Adatoms. *J. Am. Chem. Soc.* **2009**, *131*, 10473-10483.

[44] In the prior study the activation energy and reaction rate of a 0.44 wt% Au/$CeLaO_x$ catalyst resembled that of a 4.4 wt% Au/$CeLaO_x$ catalyst, that was yielded by deposition precipitation of gold and metallic gold was not leached from the catalyst.

[45] Vayssilov, G. N.; Mihaylov, M.; Petkov, P. S.; Hadjiivanov, K. I.; Neyman, K. M. Reassignment of the Vibrational Spectra of Carbonates, Formates, and Related Surface Species on Ceria: A Combined Density Functional and Infrared Spectroscopy Investigation. *J. Phys. Chem. C* **2011**, 115, 23435-23454.

[46] Hahn, K. R.; Iannuzzi, M.; Seitsonen, A. P.; Hutter, J. Coverage Effect of the CO_2 Adsorption Mechanisms on CeO_2(111) by First Principles Analysis. *J. Phys. Chem. C* **2013**, *117*, 1701-1711.

[47] Lustemberg, P. G.; Bosco, M. V.; Bonivardi, A.; Busnengo, H. F.; Ganduglia-Pirovano, M. V. Insights into the Nature of Formate Species in the Decomposition and Reaction

of Methanol over Cerium Oxide Surfaces: A Combined Infrared Spectroscopy and Density Functional Theory Study. *J. Phys. Chem. C* **2015**, *119*, 21452-21464.

[48] Elliott, B. M.; Sung, K.; Miller, C. E. FT-IR Spectra of ^{18}O-, and ^{13}C-Enriched CO_2 in the ν_3 Region: High Accuracy Frequency Calibration and Spectroscopic Constants for $^{16}O^{12}C^{18}O$, $^{18}O^{12}C^{18}O$, and $^{16}O^{13}C^{16}O$. *J. Mol. Spectrosc.* **2015**, *312*, 78-86.

[49] Fernández-Torre, D.; Kośmider, K.; Carrasco, J.; Ganduglia-Pirovano, M. V.; Pérez, R. Insight into the Adsorption of Water on the Clean CeO_2(111) Surface with van der Waals and Hybrid Density Functionals. *J. Phys. Chem. C* **2012**, *116*, 13584-13593.

[50] Molinari, M.; Parker, S. C.; Sayle, D. C.; Islam, M. S. Water Adsorption and Its Effect on the Stability of Low Index Stoichiometric and Reduced Surfaces of Ceria. *J. Phys. Chem. C* **2012**, *116*, 7073-7082.

[51] Tennyson, J.; Bernath, P. F.; Brown, L. R.; Campargue, A.; Carleer, M. R.; Császár, A. G.; Gamache, R. R.; Hodges, J. T.; Jenouvrier, A.; Naumenko, O. V.; Polyansky, O. L.; Rothman, L. S.; Toth, R. A.; Vandaele, A. C.; Zobov, N. F.; Daumont, L.; Fazliev, A. Z.; Furtenbacher, T.; Gordon, I. E.; Mikhailenko, S. N.; Shirin, S. V. IUPAC Critical Evaluation of the Rotational-Vibrational Spectra of Water Vapor. Part I-Energy Levels and Transition Wavenumbers for H_2 ^{17}O and H_2 ^{18}O. *J. Quant. Spectrosc. Radiat. Transfer* **2009**, *110*, 573-596.

[52] Zobov, N. F.; Polyansky, O. L.; Le Sueur, C. R.; Tennyson, J. Vibration-Rotation Levels of Water Beyond the Born-Oppenheimer Approximation. *Chem. Phys. Lett.* **1996**, *260*, 381-387.

[53] Lee, Y.; He, G.; Akey, A. J.; Si, R.; Flytzani-Stephanopoulos, M.; Herman, I. P. Raman Analysis of Mode Softening in Nanoparticle $CeO_{2-\delta}$ and Au-$CeO_{2-\delta}$ during CO Oxidation. *J. Am. Chem. Soc.* **2011**, *133*, 12952-12955.

[54] Guzman, J.; Carrettin, S.; Corma, A. Spectroscopic Evidence for the Supply of Reactive Oxygen during CO Oxidation Catalyzed by Gold Supported on Nanocrystalline CeO_2. *J. Am. Chem. Soc.* **2005**, *127*, 3286-3287.

[55] Lohrenscheit, M.; Hess, C. Direct Evidence for the Participation of Oxygen Vacancies in the Oxidation of Carbon Monoxide over Ceria-Supported Gold Catalysts by using Operando Raman Spectroscopy. *ChemCatChem* **2016**, *8*, 523-526.

[56] Pushkarev, V. V.; Kovalchuk, V. I.; d'Itri, J. L. Probing Defect Sites on the CeO_2 Surface with Dioxygen. *J. Phys. Chem. B* **2004**, *108*, 5341-5348.

[57] Schilling, C.; Ganduglia-Pirovano, M. V.; Hess, C. Experimental and Theoretical Study on the Nature of Adsorbed Oxygen Species on Shaped Ceria Nanoparticles. *J. Phys. Chem. Lett.* **2018**, **DOI:** 10.1021/acs.jpclett.8b02728

[58] Binet, C.; Daturi, M.; Lavalley, J.-C. IR Study of Polycrystalline Ceria Properties in Oxidised and Reduced States. *Catal. Today* **1999**, *50*, 207-225.

[59] Laachir, A.; Perrichon, V.; Badri, A.; Lamotte, J.; Catherine, E.; Lavalley, J. C.; El Fallah, J.; Hilaire, L.; Le Normand, F.; Quemere, E.; Sauvion, G. N.; Touret, O. Reduction of CeO_2 by Hydrogen. Magnetic Susceptibility and Fourier-Transform Infrared, Ultraviolet and X-Ray Photoelectron Spectroscopy Measurements. *J. Chem. Soc. Faraday Trans.* **1991**, *87*, 1601-1609.

[60] Badri, A.; Binet, C.; Lavalley, J.-C. An FTIR Study of Surface Ceria Hydroxy Groups during a Redox Process with H_2. *J. Chem. Soc., Faraday Trans.* **1996**, *92*, 4669-4673.

[61] McBride, J. R.; Hass, K. C.; Poindexter, B. D.; Weber, W. H. Raman and X-Ray Studies of $Ce_{1-x}RE_xO_{2-y}$, where RE=La, Pr, Nd, Eu, Gd, and Tb. *J. Appl. Phys.* **1994**, *76*, 2435-2441.

[62] Lakshmanan, P.; Averseng, F.; Bion, N.; Delannoy, L; Tatibouët, J.-M.; Louis, C. Understanding of the Oxygen Activation on Ceria- and Ceria/Alumina-Supported Gold Catalysts: A Study Combining $^{18}O/^{16}O$ Isotopic Exchange and EPR Spectroscopy. *Gold Bull.* **2013**, *46*, 233-242.

[63] Carrasco, J.; López-Durán, D.; Liu, Z.; Duchoň, T.; Evans, J.; Senanayake, S. D.; Crumlin, E. J.; Matolín, V.; Rodríguez, J. A.; Ganduglia-Pirovano, M. V. In Situ and Theoretical Studies for the Dissociation of Water on an Active Ni/CeO_2 Catalyst: Importance of Strong Metal–Support Interactions for the Cleavage of O–H Bonds. *Angew. Chem. Int. Ed.* **2015**, *54*, 3917-3921.